Next-generation in vivo optical imaging with short-wave infrared quantum dots

Citation: Bruns, Oliver T. et al. "Next-Generation in Vivo Optical Imaging with Short-Wave Infrared Quantum Dots." Nature Biomedical Engineering 1, 4 (April 2017): 0056 © 2017 Macmillan Publishers Limited, part of Springer Nature

As Published: http://dx.doi.org/10.1038/S41551-017-0056

Publisher: Nature Publishing Group

Persistent URL: http://hdl.handle.net/1721.1/113015

Version: Author's final manuscript: final author's manuscript post peer review, without publisher's formatting or copy editing

HHS Public Access

Author manuscript

Nat Biomed Eng. Author manuscript; available in PMC 2017 November 06.

Published in final edited form as:

Nat Biomed Eng. 2017 ; 1: . doi:10.1038/s41551-017-0056.

Next-generation *in vivo* optical imaging with short-wave infrared quantum dots

Oliver T. Bruns[1,#,*], **Thomas S. Bischof**[1,#,*], **Daniel K. Harris**[1,2], **Daniel Franke**[1], **Yanxiang Shi**[3], **Lars Riedemann**[4,5], **Alexander Bartelt**[6], **Frank B. Jaworski**[7], **Jessica A. Carr**[1], **Christopher J. Rowlands**[8], **Mark W.B. Wilson**[1,9], **Ou Chen**[1,10], **He Wei**[1], **Gyu Weon Hwang**[1,2,11], **Daniel M. Montana**[1,2], **Igor Coropceanu**[1], **Odin B. Achorn**[1], **Jonas Kloepper**[4], **Joerg Heeren**[12], **Peter T.C. So**[7,13], **Dai Fukumura**[4], **Klavs F. Jensen**[3], **Rakesh K. Jain**[4], and **Moungi G. Bawendi**[1,*]

[1]Department of Chemistry, Massachusetts Institute of Technology, 77 Massachusetts Ave., Cambridge, MA 02139 (USA)

[2]Department of Materials Science and Engineering, Massachusetts Institute of Technology, 77 Massachusetts Ave., Cambridge, MA 02139 (USA)

[3]Department of Chemical Engineering, Massachusetts Institute of Technology, 77 Massachusetts Ave., Cambridge, MA 02139 (USA)

[4]Edwin L. Steele Lab for Tumor Biology, Massachusetts General Hospital and Harvard Medical School, 100 Blossom St., Boston, MA 02114 (USA)

[6]Department of Genetics and Complex Diseases and Sabri Ülker Center, Harvard T.H. Chan School of Public Health, 665 Huntington Ave., Boston, MA 02115 (USA)

[7]Raytheon Vision Systems, Goleta, California 93117 (USA)

[8]Department of Biological Engineering, Massachusetts Institute of Technology, Cambridge, Massachusetts (USA)

[*]Correspondence to: obruns@mit.edu, tbischof@mit.edu and mgb@mit.edu.

[#]Both authors contributed equally

[5]Present address: Neurology Clinic and National Center for Tumor Diseases, University Hospital Heidelberg, and Clinical Cooperation Unit Neuro-Oncology, German Cancer Consortium, German Cancer Research Center, 69120 Heidelberg, Germany.

[9]Present Address: Department of Chemistry, University of Toronto, 80 St. George Street, Toronto, ON M5S 3H6 (Canada)

[10]Present Address: Department of Chemistry, Brown University, Providence, RI 02912 (USA)

[11]Present Address: Korea Institute of Science and Technology, Seoul, 02792, (Republic of Korea)

Author contributions

O.T.B., T.S.B., D.K.H., D.Franke, L.R., A.B., F.B.J., J.A.C., M.W.B.W., O.C., H.W., G.W.H., D.M.M., I.C., O.B.A., J.K. performed.the experiments, O.T.B, T.S.B., Y.S., C.J.R. analysed the data, O.T.B., T.S.B. and M.G.B. wrote the paper and were assisted by D.Franke, A.B. and R.K.J.. J.H., P.T.C.S, D.Fukumura, K.F.J., R.K.J. provided guidance on the study design. J.H., provided lipid samples. All authors reviewed and edited the manuscript.

Competing Financial Interests

The authors declare no competing financial interests

Code availability

The code for particle image velocimetry was written in Matlab 2015a and is available at https://github.com/massivehair/PIV

Data availability

All raw and processed-image data generated in this work, including the representative images provided in the manuscript, are available from the corresponding authors on reasonable request.

[12]Department of Biochemistry and Molecular Cell Biology, University Medical Center Hamburg-Eppendorf, Martinistrasse 52, 20246 Hamburg, Germany

[13]Department of Mechanical Engineering, Massachusetts Institute of Technology, Cambridge, Massachusetts (USA)

Abstract

For *in vivo* imaging, the short-wavelength infrared region (SWIR; 1000–2000 nm) provides several advantages over the visible and near-infrared regions: general lack of autofluorescence, low light absorption by blood and tissue, and reduced scattering. However, the lack of versatile and functional SWIR emitters has prevented the general adoption of SWIR imaging by the biomedical research community. Here, we introduce a class of high-quality SWIR-emissive indium-arsenide-based quantum dots (QDs) that are readily modifiable for various functional imaging applications, and that exhibit narrow and size-tunable emission and a dramatically higher emission quantum yield than previously described SWIR probes. To demonstrate the unprecedented combination of deep penetration, high spatial resolution, multicolor imaging and fast-acquisition-speed afforded by the SWIR QDs, we quantified, in mice, the metabolic turnover rates of lipoproteins in several organs simultaneously and in real time as well as heartbeat and breathing rates in awake and unrestrained animals, and generated detailed three-dimensional quantitative flow maps of the mouse brain vasculature.

Introduction

In order to understand the molecular and cellular mechanisms involved in physiology and disease, biomedical research increasingly aims toward non-invasive imaging with cellular resolution *in vivo*. Fluorescent probes in particular can be detected with very high sensitivity, ultimately allowing the resolution and tracking of single labeled biological entities. This enables the study of rapid biological processes in greater detail than other imaging modalities, such as magnetic resonance imaging (MRI), ultrasound (US) or computed tomography (CT)[1]. However, when imaging whole organisms several biological obstacles remain which reduce the sensitivity, acquisition speed, and spatial resolution of fluorescence imaging. Autofluorescence of tissue or cells adds a background signal, decreasing the contrast and therefore the sensitivity; absorption and scattering of the excitation and emission light by blood and other tissue limits signal detection and impacts acquisition speeds; and scattering limits the spatial resolution as a function of depth, causing blurring of the acquired image.

Imaging in the short-wavelength infrared region (SWIR; 1000—2000 nm) addresses all of these challenges simultaneously. The minimal autofluorescence of biological tissue in the SWIR region leads to increased sensitivity[2,3], while the significantly reduced light attenuation from scattering and from absorption from blood and other structures enables imaging with high spatiotemporal resolution and penetration depth[3–9]. Consequently, large organisms like a whole mouse may be rendered translucent when imaged using SWIR fluorescence[4,8,10].

Thus far, the lack of a versatile SWIR emitter technology has prevented the general adoption of SWIR *in vivo* imaging despite its advantages over visible and near-IR imaging. Versatile probes ideally need to combine a high fluorescence quantum yield (QY) for sensitive and fast imaging, a tunable and narrow emission to generate different colors for multiplexing, and biocompatible functionalizations for specific biological imaging applications.

Here we introduce SWIR-emitting InAs-based core/shell (CS) and core/shell/shell (CSS) quantum dots (QDs) as a versatile class of materials for functional biological imaging (Figure 1). These InAs-based QDs exhibit a dramatically higher QY and stability than previously described SWIR probes[2,3,8,9,11–17], as well as a narrow and size-tunable emission spectrum comparable to established visible-light emitting QDs[18]. To demonstrate some of the capabilities of this imaging platform, we present three different surface functionalization (Figure 1) which we use in specific applications: SWIR QD nanosomes, which are labelled lipoproteins, allow the direct quantification of metabolic processes in real time by non-invasively imaging their transition between brown adipose tissue (BAT), blood, and liver. Long-circulating SWIR QD phospholipid micelles enable assessment and quantification of heart rate and respiration of both sedated and awake mice. With SWIR QD composite particles we perform angiography in the brain of a mouse, directly identifying arteries and veins. Furthermore, these SWIR QD composite particles enable us to quantify blood flow in the vasculature of the brain by tracking individual composite particles during intravital microscopy, which allows the visualization of the dramatic differences between blood flow in healthy vasculature and in vessels at the tumor margin, with sufficient spatial and time resolution to measure flow in individual capillaries. In summary, InAs-based QDs excel compared to commonly employed SWIR probes through improved optical properties and easy functionalization. This class of probes is a promising candidate for use in the next generation functional SWIR imaging applications.

Results

Characterization of core/shell and core/shell/shell QDs and their functional surface modifications

A synthesis scheme based on a continuous injection approach[19] allows us to synthesize large, SWIR-emissive InAs core QD with improved optical quality and improved thermal stability through slow crystal growth at high temperatures. These InAs cores exhibit a narrow size distribution of 4.3 nm +/− 0.4 nm (10%) and exhibit the zinc blende crystal structure of the bulk material (Supplementary Figure 1). We employed these InAs cores as starting material to be overcoated with shells consisting of higher band gap materials, to yield various InAs core/shell (CS, InAs/CdSe and InAs/CdS) and core/shell/shell (CSS, InAs/CdSe/CdSe and InAs/CdSe/ZnSe) QDs with broad absorption and bright and photostable emission (Supplementary Figure 2–3, Supplementary Note 1). The emission of the resulting CS and CSS QDs allow us to cover the entire range of the sensitivity range of modern SWIR cameras from 900 nm to 1600 nm (Figure 2a). Exemplary CSS particles are monodisperse with a size distribution as narrow as 8% (Figure 2b, Supplementary Figure 4). As a result of employing this new generation of InAs cores as starting materials our resulting CS and CSS QDs exhibit improved QYs, especially at longer wavelengths. Supplementary

Figure 5 shows that samples typically exhibit QYs of 10—20% in physiological saline solution and remain as photostable colloidal nanocrystals over several months. With a QY of 30% for our best sample, the QYs of our probes are more than one hundred times higher than those of commonly used carbon nanotubes (CNTs; 0.1%, Supplementary Note 2) and roughly 10 times higher than the best performing SWIR emitting materials previously applied to biological imaging[8,9,11,13–17,20] (Figure 2c). To transfer the prepared CS and CSS QDs into aqueous media and to demonstrate functional imaging with SWIR QDs, we employ three different surface coatings (Figure 1). Phospholipid micelles allow long blood circulations times (Supplementary Figure 6) and thus enable angiography and related applications such as vital sign monitoring[21,22]. QDs incorporated into lipoproteins (SWIR QD nanosomes) enable imaging the energy metabolism of activated tissues and organs in real time. Lastly, we employ large SWIR QD composite particles that are bright enough for single particle tracking during SWIR intravital microscopy, which allows us to generate large-scale three-dimensional blood flow maps for a quantitative description of local tissue microenvironments. Figures 2 d–f show that the emission spectra of our probes are only slightly affected by the phase transfer, and high QYs are maintained upon phase transfer into physiological buffer. Characterization of size and size-distribution show small, monodisperse QD phospholipid micelles (21 nm) and larger QD nanosomes (around 300 nm) and QD composite particles (around 350 nm) with moderate size distributions (Supplementary Figure 7). Supplementary Figure 8 shows that all three surface functionalizations yield probes with slightly negative zeta potentials. Our library of CS and CSS QDs with narrow emission linewidths and tunable emission readily allows the acquisition of multiple colors in the SWIR band (Figure 2g and 2h, and Supplementary Video 1). In addition to a high QY, our CS and CSS QDs exhibit short, excitation wavelength-independent photoluminescence lifetimes on the order of 100 ns (Supplementary Figure 9), which is about one order of magnitude faster than comparable PbS-based QDs. This emission characteristic is important for high-flux applications such as confocal microscopy, as the PL lifetime sets both the maximum excitation flux before saturation is reached and the limit on overall emission output.

Metabolic Imaging with SWIR QD Nanosomes

We and others have recently incorporated visible light-emitting QDs into lipoproteins to follow their physiologic fate *in vivo*[23–27]. Lipoproteins, in particular triglyceride-rich lipoproteins such as chylomicrons, which are micron size micelles, carry dietary lipids absorbed by the intestine through the lymphatic system into the blood stream and deliver their cargo to peripheral tissues such as brown and white adipose tissue, skeletal muscle, and the heart. Similar to glucose, triglyceride-rich lipoproteins are a major source of energy for tissues. Therefore labeled lipoproteins (SWIR QD nanosomes) allow studying metabolic activity complementary to flurodeoxyglucose (18F) glucose positron emission tomography (FDG PET) imaging.

Existing methods such as MRI or radioactive labeling are limited by either their sensitivity and dynamic range or their temporal resolution and invasive nature. The relative transparency of tissues at SWIR wavelengths enables tracking of labeled lipoproteins as they circulate and bind to the vasculature of target organs. Additionally, the relative lack of

autofluorescence from these tissues enables the detection of low lipoprotein concentrations, and thus allows for quantification within a large dynamic range. Brown adipose tissue (BAT) is a heat-producing organ, which in response to cold exposure fuels its high metabolic activity by the uptake of triglyceride-rich lipoproteins[24]. To characterize this process, we exposed wild-type mice (4 biological replicates) to 4°C for 24 hours to activate their BAT. After sedation and preparation, individual mice were illuminated with an 808 nm source (15 mW/cm^2), and were injected with SWIR QD nanosomes - labeled recombinant chylomicrons - via the tail vein at a constant rate of 26.7 μL/min for 9.3 minutes (0.267 mg triglycerides/min, 13.3 pmol QDs/min); Figure 3a and Supplementary Video 2). During and after the injection we imaged the SWIR emission. The time response of the emission intensity arising from BAT, peripheral vasculature, and the tail vein (Figure 3b) was then analyzed. The emission intensity in each region of interest provides a measure of the relative concentration of the labeled chylomicrons at that location, and halting the injection enables capturing the kinetics of the physiological metabolic processes in each organ. The emission intensity for the brown adipose tissue is detected with subsecond resolution and a noise level of 56 counts. We observed an increase of the emission in brown adipose tissue at a rate of 430 counts/sec during the injection of 13.3 pmol QD/min or 222 fmol QD/sec. Therefore we estimate that we can detect with a sensitivity of 86 femtomol to achieve an SNR of 3. This imaging paradigm is robust and technically highly accurate as the biological variation between four replicates could be clearly measured and was not overcome by noise of the measurement (Supplementary Figure 10). Figure 3b overlays the results to show the reproducibility and biological variation between individual mice.

From these kinetic traces we are able to measure the blood half-life and rate at which chylomicrons are released from the BAT as chylomicron remnants. After the injection into the tail was halted the particles cleared from the blood and the signal decay for peripheral vasculature is fit well by a sum of two exponential functions and a constant. The blood half-life is on the order of 1 minute (73 ± 1 s; 42 ± 1 s; 70 ± 3 s; 58 ± 3 s) which is in agreement with previously reported values for cold-exposed mice based on radioactive labeling[24]. The signal from the BAT decayed significantly slower and is fit well by a sum of two exponential functions. The signal remaining in the BAT revealed that initial release of chylomicrons remnants, the product of lipolysis, from this tissue occurred with a time constant of about 3 minutes (196 ± 5 s; 83 ± 1 s; 195.5 ± 0.5 s; 241.0 ± 0.5 s; roughly half of the bound chylomicron population was cleared in this way). This is followed by a much slower decay on a time scale of greater than 30 minutes (roughly half of the bound chylomicron population showed this behavior). The long residence time is consistent with recent reports noting the existence of long-term uptake of particles[24]. The particles released from the BAT and other peripheral tissues are then cleared by the liver.

The SWIR region offers three benefits in this application: First, the longer penetration length allows us to resolve the image of organs deep in a mouse; second, as tissues are translucent in this region, small concentrations of SWIR QDs can be detected with high temporal resolution even with a relatively low excitation flux; and, finally, the relative absence of tissue autofluorescence enables the highly sensitive detection of concentrations down to the femtomolar regime and thus allows quantification over a large dynamic range.

High-speed whole body imaging using QD phospholipid micelles

The high QYs of our QDs, coupled with the fact that tissues are translucent in the SWIR, gives rise to high emission signals even under low excitation fluxes. This allows us to image at acquisition speeds of up to 66.5 frames per second (fps) — limited not by signal but by the readout electronics of our camera — while retaining high resolution and good signal-to-noise at a safe excitation flux. The high QYs allow an acquisition speed that is more than twice as fast than in previous reports for imaging in the SWIR[11] with a resolution that has four times more pixels, resulting in 10-fold increase of pixel throughput (Supplementary Table 1). Figure 4 and Supplementary Videos 3–5 show whole body imaging of mice, both anesthetized as well as awake and unrestrained, demonstrating the high speed and high signal-to-background ratio of our SWIR QDs. Indeed, we measure a signal for the heart and liver that is more than two orders of magnitude higher than background autofluorescence, and a signal-to-noise ratio for the liver of about 250 or 24 dB for our 640×512 pixel camera (Figure 4b, Supplementary Videos 3–4). Both heartbeat and the respiratory cranio-caudal motion of the liver (Figure 4b and Supplementary Video 4) are clearly resolved. This representative anesthetized mouse shows a respiratory rate of 84 breaths per minute (Figure 4c) and a heart rate of 130 beats per minute (Figure 4d).

Physiology however, is profoundly affected by anesthesia. Currently used approaches to record the heart rate in awake animals rely either on implanting telemetric sensors by surgery or by ECG after confining the animal in a device with conductive pads for recording. The emission of SWIR QDs signal can overcome this limitation and is in fact strong enough to study freely moving and awake mice, in contrast to stationary and anesthetized mice which are required for most other imaging techniques such as MRI, CT and US. We injected long-circulating SWIR QD phospholipid micelles via the tail vein into awake mice and placed them into our imaging setup. After allowing the mice to acclimate, we imaged in the dark, reflecting their usual environment as a nocturnal species. Notably, the 808 nm laser used in this experiment is invisible to mice, as their eyes are even less sensitive than humans' to these wavelengths[28]. Figure 4e (Supplementary Video 5) demonstrates our ability to measure the heart and respiratory rates of a mouse, in a contact-free way and without restraining or otherwise affecting the mouse. The recorded heart and respiratory rates at rest of this representative mouse were 300 breaths per minute (Figure 4f) and 550 beats per minute (Figure 4g), in agreement with the literature[29,30] (SWIR QD whole body imaging was reproducibly performed on more than 10 mice). *In vivo* imaging in the SWIR using high-QY QDs thus opens up the possibility of contact-free non-invasive physiological imaging of mice that are awake and undisturbed.

One-photon excitation SWIR intravital microscopy using SWIR QD composite particles

The SWIR region of the optical spectrum is also optimal for intravital microscopy. The SWIR region benefits from long wavelength excitation in the near-infrared (NIR) similar to multi-photon microscopy, allowing deep tissue penetration and relatively high excitation flux without tissue damage. But there is one important difference: Multi-photon microscopy relies on two or three photons combining to create a non-linear excitation event in a fluorophore that then emits in the visible range. This process is seven to eight orders of magnitude less efficient than emission from single photon excitation. The ability to excite in

the near-IR with a one-photon event and detect in the SWIR gives rise to bright emission at moderate excitation intensities (on the order of 10 W/cm^2 in our set-up). In comparison, the peak intensity in the focus of multi-photon microscopes is on the order of 10^6–10^{12} W/cm^2. Additionally we benefit from the virtual absence of tissue autofluorescence and the high transmission of the SWIR emission. This combination allows us to easily generate microscopic images at video rate at penetration depths similar to multi-photon microscopy with an epifluorescence approach.

We used these benefits of SWIR imaging with QDs to image a glioblastoma (GBM) tumor growing in a mouse brain through a transparent cranial window (Figure 5a). In this experiment the tumor was pre-labeled by injection of the SWIR QD composite particles three days before imaging. Following pre-labeling, the tumor continued to grow and the long-circulating SWIR QD composite particles are seen to accumulate in collapsed and abnormal tumor blood vessels (Figure 5b). A second dose of the SWIR QD composite particles was injected and perfusion was imaged at video-rate across the entire cranial window (30 fps, Supplementary Video 6). The time series of images was then deconvolved into the pre-labelled tumor (Figure 5b), the arterial vessels (Figure 5c) and the venous vessels (Figure 5d), using a form of principal component analysis[31]. The resulting color-coded image (Figure 5e) demonstrates how the growing tumor affects the vascular network.

Generating quantitative blood flow maps using QD composite particles

We further demonstrate that SWIR QD composite particles allow detailed and quantitative imaging of blood flow in relatively large tissue volumes. Quantification of blood flow in the brain is of great importance as it serves as a surrogate for metabolic activity (e.g. in functional MRI (fMRI)). Aberrant blood flow in diseases ranging from cancer to stroke often leads to hypoxia. Current approaches to measure blood flow either lack the spatial resolution to resolve individual capillaries (e.g. fMRI) or are too slow to acquire flow information of large volumes (e.g. line-scanning multi-photon microscopy[32]).

Z-sectioned images of abnormal and normal vasculature in the same mouse (Figure 6a) were generated by imaging the dynamics of the flow in healthy tissue (Supplementary Video 7) and in the tumor margin of a GBM (Supplementary Video 8). The GBM tumor margin shows irregular blood flow, including oscillatory “pendular” flow, while the healthy tissue in the contralateral brain hemisphere shows a normal vessel network with regular blood flow. Calculating the maximum projection of all frames visualizes the overall structure of the vasculature in the tumor margin (Figure 6b) and healthy tissue (Figure 6c). The details of the vessel structure, however, are confounded by out-of-plane information. Subtracting the average signal of these 600 frames from the maximum intensity projection isolates the signal in the focus originating only from individual SWIR QD composite particles (Figures 6d–e).

In another approach to enhance the contrast of the focal plane and provide true z-sectioning capability, we calculated the sum of the magnitude of the difference of each frame from the average, which is sensitive only to fluctuations in time, i.e. the transit of individual composite particles. The static z-sectioned images produced in this fashion are comparable to equivalent images produced using multiphoton microscopy (MPM). Figures 6f–k directly compare the micrographs of the same fields of view of a healthy mouse brain at various

depths, using our z-sectioning approach (Figures 6f–h) and conventional MPM (Figures 6i–k).

We also exploited the unprecedented high spatiotemporal resolution of our data to perform particle image velocimetry (PIV)[33–36], yielding z-sectioned measurements of the flow of blood through the vasculature at 5 μm increments (Supplementary Figure 11 and Supplementary Video 9). By combining static images of the vasculature in the healthy and the tumor margin part of the mouse brain shown in Figure 5 and 6 (Figures 7a,b and Supplementary Videos 7 and 8) with their flow information (Figures 7c,d), we generated a quantitative representation of blood flow in the tumor margin and healthy brain. This can be extended to a three-dimensional representation of blood flow in the brain as shown for representative healthy mice (Supplementary Figure 11 and Supplementary Videos 9, 10, 11 and 12) (SWIR QD intravital microscopy with composite particles was performed for different organs in more than ten mice). Each z-section requires 10 sec of experimental time (Supplementary Video 10), so that large volumes of brain tissue may be mapped in minutes. The high spatial and velocity resolution of our flow maps arise directly from our ability to accurately measure the motion of individual particles over time, which is only achievable through the use of bright and compact labels, such as the here presented SWIR QD composite particles.

In vivo safety and toxicological profiles of SWIR QDs

To examine the safety of SWIR QDs in vivo, C57/BL6 mice were administered a single intravenous dose of SWIR QD phospholipid micelles, SWIR QD composite particles, or isotonic sodium chloride as a control (7 mice per group). Body weight was measured over the following days and blood and organs were collected 6 days later to assess acute toxicology. There was no difference in body weight gain between the three groups injected with QD phospolipid micelles, QD composite particles or isotonic sodium chloride. No hepatotoxicity was observed, as there was no difference between the three groups in the levels of alkaline phosphatase, alanine aminotransferase, aspartate aminotransferase, total bilirubin and albumin. Furthermore, no nephrotoxicity was observed, as there was no difference between the three groups in the levels of blood urea nitrogen, creatinine, calcium, phosphorus, chloride, potassium and sodium. In addition, a complete blood count was performed to identify signs of haematological toxicity. The results showed no differences between the three groups for leukocyte count, red blood cell count, platelet count, hemoglobin levels and hematocrit (Supplementary Table 2).

The SWIR emission from the particles was still present after 6 days, which indicates that the particles are long-term stable *in vivo* under physiological conditions. Emission from both the QD phospholipid micelles and QD composite particles were exclusively found in the liver and spleen after 6 days, while other organs such as the lungs, kidneys, and the heart showed no emission signal, indicating clearance via liver and spleen. In summary, SWIR QD particles exhibit excellent *in vivo* stability and show no signs of toxicity 6 days after injection.

Discussion

The SWIR spectral range has previously been introduced as a spectral regime where living tissue can become translucent, thus for example allowing the observation of brain vasculature through skin and skull of mice using fluorescence imaging[4]. However, the lack of a versatile SWIR emitter technology has prevented the general adoption of SWIR *in vivo* imaging despite its advantages over visible and near-IR imaging. Here, we demonstrate that combining a new generation of InAs-based CS and CSS SWIR QDs with high QYs with a class of three surface coatings allows for functional biomedical *in vivo* imaging of both sedated and awake animals, yielding detailed information about metabolism, physiology, and pathologic processes such as tumor angiogenesis.

In one class of applications, the deep penetration of SWIR emission and the low levels of background enable us to directly measure metabolic activity with femtomolar sensitivity in different tissues in a mouse by tracking SWIR QD labeled lipoproteins. In contrast to existing methods based on radioactive labelling our technique allows measuring the kinetics with a precision of a few seconds that exceeds the biological variation between mice of the same group (on the order of tens of seconds). With this method it is now possible to completely measure, in real-time and with high dynamic range, lipoprotein processing for several organs simultaneously in individual mice. We anticipate future work in which the individual mechanisms of binding and uptake can be analyzed in greater detail in individual animals, possibly reducing the required amount of biological replicates for quantitative studies. It is also possible to assess the real-time effects of an intervention within an individual animal, such that the results are purely reflective of the effects on the individual and not biased by differences within the population. This approach is not limited to lipoproteins but can be expanded to study the binding kinetics of therapeutic antibodies or other biomolecules.

In a second class of applications, the orders-of-magnitude improvement of signal and long blood circulation lifetimes that QD phospholipid micelles provide, relative to existing SWIR probes, enable imaging physiological processes that are otherwise too fast to be detected by common imaging methods such as MRI or near-infrared fluorescence imaging. We demonstrate the measurement of the heartbeat and breathing rates of an awake and unrestrained mouse, paving the way for automated and unobtrusive monitoring of animals in their normal environments. This method could be applied to test drug candidates for cardiac arrhythmia, for which SWIR imaging would enable researchers to monitor the animals over time without the need to implant telemetric devices. The ability to non-invasively monitor vital signs would also be beneficial for studies of exercise and behavior, where it is critical to ensure that the animal is in a normal and unstressed state.

In a third class of applications in a microscopic setting, the strong signal of our QD composite particles enables the measurement of blood flow in the vasculature of the brain. With this method, it is possible to quantify the flow in large volumes of vasculature in only a few minutes of experimental time, for example before and after an intervention to study ischemia-reperfusion in stroke. The applications, however, are not limited to pathological processes: almost every tissue can switch between a baseline, resting state, and an activated

state of enhanced functional performance (motion of a muscle, lipolysis of white adipose tissue, heat production by BAT) with increased perfusion. Similar to functional MRI but with much higher spatial and temporal resolution our technique of flow measurement may allow quantification and tracking of the activation of certain areas of the brain by detecting changes in blood flow in response to external stimuli.

Central to all of these applications is our ability to appropriately functionalize QDs. Even an emitter with superior optical properties is rendered useless if it cannot be tailored for a given application. The toolkit of SWIR QDs and surface modifications that we present paves the way for a widespread adoption of SWIR *in vivo* imaging in the pre-clinical setting. While we did not observe toxic effects in mice during our short-term studies we realize that the chemical composition of our SWIR QDs likely prohibit their use in humans. Thus the development of heavy metal-free, high quality SWIR emitters will be the next challenge in order to bring SWIR imaging into clinical settings. In the meantime, our versatile functional SWIR emitter toolkit opens an avenue toward the broader application of SWIR imaging in biomedical research.

Methods

Synthesis of InAs core/shell QDs

To synthesize QD samples that span the entire SWIR region both size- and composition-tunability of InAs-based QDs was used.

In general the InAs core sets the initial wavelength and our synthetic approach allows us to synthesize cores with emission from around 700–1200 nm. To access emission wavelengths >1200 nm, InAs cores were overcoated with either CdSe or CdZnS.). In some cases these core-shell QDs were enclosed with an outer shell consisting of a higher bandgap material such as ZnSe or CdS.

Synthesis of InAs cores—In a typical procedure, 4 mmol of indium(III) acetate, 14 mmol myristic acid, and 20 mL 1-octadecene were added to a 50 mL 4-neck round bottom flask. The flask was heated to 110°C under vacuum (10 mtorr) for two hours to remove acetic acid and form a solution of indium(III) myristate. The indium myristate solution was heated under argon to 295°C. An injection syringe containing 0.22 mmol tris(trimethylgermyl)arsine dissolved in 4 mL tri-n-octylphosphine was prepared in a nitrogen glovebox and rapidly injected into the indium myristate solution at 295°C. After 10 minutes, a syringe containing 0.72 mmol tris(trimethylgermyl)arsine dissolved in 1 mL tri-n-octylphosphine and 4 mL 1-octadecene was loaded into a syringe pump and the arsenic precursor solution was injected at 4mL/hour at a temperature of 295°C. The QD size was monitored during this step by removing aliquots from the solution. When the QDs reached the desired size, the precursor injection was stopped and the reaction was removed from heat.

The QDs were isolated by filtering the growth solution diluted in toluene through a 200nm PTFE filter, then adding acetone to cause the QDs to precipitate out of solution and

centrifuging. The QDs were dissolved in 20mL hexane and stored for overcoating (See Supplementary Figure 1 for results of characterization of InAs QDs).

Overcoating InAs QDs

InAs/CdSe/ZnSe: The ZnSe overcoating procedure is adapted from a published method[37]. 44 nmol of InAs cores in hexane were added to 4 mL of 1-octadecene, 3 mL of oleylamine, and 0.5 mL of 0.05 M trioctylphosphine selenide in TOP (TOPSe). The solution was degassed at 100°C under vacuum for 40 minutes, 15 mtorr, to remove the hexane, and then heated to 230°C under argon. 0.47 mL of solutions of 0.05 M cadmium oleate and 0.05 M TOPSe were injected side by side using a syringe pump at 1 mL/hr at 230°C. Then 0.6 mL of 0.05 M diethylzinc was added and the temperature was raised to 250°C. After 15 minutes, 0.6 mL of 0.05 M TOPSe was added. After 15 minutes, 0.75 mL of 0.05 M diethylzinc was added. After 10 minutes, 0.95 mL of 0.04 M Se dissolved in ODE was added. After 15 minutes, 1 mL of oleic acid was injected. After 13 minutes, 0.95 mL of diethylzinc was added. After another 13 minutes, 1.2 mL of 0.04 M ODE-Se was added. The temperature was raised to 290°C for 25 minutes and then the reaction mixture was cooled. The quantum yield was found to be 30% using an integrating sphere. The PL peak was around 1075 nm.

InAs/CdS: This procedure is adapted from conditions described for making CdSe/CdS core/shell QDs[38]. 90 nmol of InAs cores in hexanes were added to 10 mL of ODE. The solution was degassed under vacuum at 100°C to remove the hexane. 8.2 mL of 0.05 M solutions of cadmium oleate and sulfur in 1-octadecene were added side by side using a syringe pump at 5 mL/hr at a temperature of 230°C. The PL peak was found to be 1150 nm, with a quantum yield of 35% in chloroform.

InAs/CdSe: Overcoating of InAs with CdSe was adapted from.[20]. 30 nmoles of 4.95nm diameter InAs cores in 1mL of hexane was dissolved in 3mL of ODE and 2mL of oleylamine. Vacuum was applied at room temperature to remove the hexane, and then the solution was briefly turned to argon in order to add 0.8mL of 0.05M TOPSe (about 1 monolayer (ML) worth of Se) in ODE to the reaction. The solution was heated to 100°C for 1 h under vacuum, before turning to argon and heating to 220°C. Syringes of 0.045M of cadmium(II) myristate in TOP and 0.05M TOPSe in ODE were prepared in air, and after the solution reached 220°C, the cadmium(II) myristate and TOPSe solutions were added to the solution via syringe pump at a rate of 2mL/h. During the overcoating, the PL peak shifted from 1080nm to 1420nm. The large redshift observed here is due to the loss of confinement due to the low conduction band o set between CdSe and InAs resulting in pseudo-type II behavior. After purification by acetone precipitation, the PL peak was found to blueshift to 1380nm. The QY of the purified solution was measured to be 7 % with a FWHM of 250nm. This reaction was designed to add about 6ML to the InAs cores. Similar procedures were performed to produce particles with bluer wavelengths by using 1.5ML and 3ML.

InAs/CdSe/CdS: InAs/CdSe/CdS QDs were prepared as previously described[19]. Briefly, purified InAs QDs (96 nmoles, diameter of 4.7 nm, PL emission at 1039 nm) in hexanes were transferred to a mixture of ODE (3 mL) and oleylamine (3 mL) in a four neck flask. The mixture of ODE and oleylamine was previously degassed at 115°C for at least one hour.

The solution was switched to vacuum to remove the hexanes for 30 minutes at RT and another 10 minutes at 110°C. Subsequently, the solution was heated to 280°C for the shell growth. As soon as the mixture reached 240°C, shell precursor injection was started using 0.05 M shell precursor solutions in ODE. Cd(Ol)2 (111 μmoles) and TOPSe (111 μmoles) were added over the course of 67 minutes (injection speed 2 mL h^{-1}). InAsCdSe CS QDs were purified using the above described procedure (however using acetone and methanol as non-solvents) and stored in hexanes. In contrast to bare InAs cores the InAs core-shell QDs were not transferred to a glovebox but stored in air. The size was measured to be 5.1 nm (TEM) and the QDs exhibited a PL peak at 1296 nm. The resulting InAsCdSe (roughly 86 nmoles, 10% loss through aliquots and purification) were redispersed in ODE (3 mL) and oleylamine (3 mL), and degassed at RT for 30 minutes and at 100°C for 10 minutes. To that solution 3 mL of a 0.05 M Cd(Ol)2 and 3 mL of a 0.045 M sulfur solution in ODE were added (150 μmoles Cd and 135 μmoles S) at 240°C within one hour. The final QD diameter was determined to be 6.9 nm (TEM) with a PL emission at 1307 nm. Elemental analysis using EDS showed that the following elements ratios:In:As = 1.0 (Theoretical 1.0), Cd:(Se +S)=1.2 (Theoretical 1.1), S:Se = 1.9 (Theoretical 1.4), Cd:In = 7.0 (Theoretical 3.0)

Synthesis of PbS/CdS core/shell QDs

PbS is synthesized with lead oleate as a Pb precursor, hexamethyldisilithiane (as known as $(TMS)_2S$) as a S precursor, and 1-octadecene as a solvent[39]. All the syntheses were performed under an inert atmosphere. Lead oleate is prepared using lead acetate trihydrate and oleic acid at 120 °C, then the lead precursor is heated to 150 °C under nitrogen before injection of the sulphur precursor. After cooling to room temperature, this solution is transferred into a nitrogen-filled glove box without air exposure. The synthesized PbS QDs are purified three times by adding methanol and 1-butanol until the solution is turbid, followed by centrifugation to precipitate the QDs. The supernatant is discarded and the QDs are re-dissolved in hexane. PbS/CdS core/shell QDs are prepared by cation-exchange[40,41] at 100 °C for 5 min under nitrogen using an excess of cadmium oleate. PbS/CdS core/shell QDs are also precipitated with ethanol and re-dissolved into hexane three times to purify and remove unreacted precursors.

See Figure 2 and Supplementary Figure 2–4 for results of characterization of the different core-shell and core-shell-shell QDs.

Phase transfer and surface modification

QD phospholipid micelles—QDs were transferred into aqueous buffers using a previously reported procedure[21,22]. Briefly, 2 mg (dry weight) QDs were mixed with 25 mg 18:1 PEG2000 PE (1,2-dioleoyl-sn-glycero-3-phosphoethanolamine-N-[methoxy(polyethylene glycol)-2000]) (ammonium salt) (Avanti Polar Lipids; Cat.No 880130) in chloroform. After brief sonication for 10 seconds the solvent was removed under nitrogen flow and 2 mL isotonic saline or water were added. To completely solubilize the QDs the aqueous solution was sonicated with a probe sonicator for 5 min. This solution was filtered through a 0.2 μm filter.

QD nanosomes (QD-labelled recombinant triglyceride rich lipoproteins)—QD-labelled recombinant triglyceride rich lipoproteins were generated by a previously reported procedure[23,24]. Briefly, physiological lipoprotein extracts from triglyceride rich lipoproteins (TRL) were extracted by the method of Folch[42]. For incorporating the QDs into the recombinant lipoproteins, 20 mg of the lipid extract (approximately 80% triglycerides, 10% cholesterol and 10% phospholipids) were dissolved in chloroform and mixed with 1 mg (dry weight) InAs core/shell nanocrystals. The solvent was removed and TRL were formed in 2 mL PBS or isotonic saline by sonication with a probe sonicator for 10 minutes. Potential aggregates were removed by filtration using a 0.45 μm filter prior to intravenous injection (2 mg lipid per mouse).

QD composite particles—To obtain composite particles with a long circulation time 2 mg (dry weight) QDs were mixed with 5 mg 18:1 PEG2000 PE (1,2-dioleoyl-sn-glycero-3-phosphoethanolamine-N-[methoxy(polyethylene glycol)-2000]) (ammonium salt) (Avanti Polar Lipids; Cat.No 880130), 80 mg soy bean oil and 1.4 mg phosphatidylcholine in chloroform. After brief sonification for 10 seconds the solvent was removed under nitrogen flow and 2 mL isotonic saline were added. To form an emulsion of composite particles the aqueous solution was sonicated with a probe sonicator for 10 minutes. This solution was filtered through a 0.45 μm filter, yielding a solution of particles which were roughly 400 nm in diameter with a broad size distribution.

See Supplementary Figure 5–8 for results of characterization of the different functionalizations.

Optical characterization of QDs

Photoluminescence quantum yield (QY)—Quantum yield measurements were obtained using an integrating sphere (Labsphere RTC-060-SF). The sample was illuminated using a 785nm diode laser with an excitation power of 25mW that was chopped at 210 Hz. The output was collected using a calibrated germanium detector (Newport: 818-IR) through a Stanford Research Systems lock-in amplifying system. An 800 nm colored glass longpass filter was used to block the excitation beam. The sample was placed in a PTFE capped quartz cuvette and a solvent blank was used to ensure as uniform of an environment inside the integrating sphere as possible. The measured photocurrent was adjusted to account for the external quantum efficiency of the detector when calculating the quantum yield. Finally, the measured quantum yield was corrected to account for leakage of the excitation light and the transmittance of the filter.

Photoluminescence spectroscopy—For samples with emission peaks between 900 nm and 1300 nm, a single-grating spectromter (Acton; SpectraPro 300i) was used in conjunction with a liquid nitrogen cooled InGaAs line camera (Princeton Instruments; OMA V, 512×1 pixels). Samples were excited with a 532 nm diode laser, and emission was collected using a pair of gold-coated off-axis parabolic mirrors.

Photoluminescence lifetime—To measure photoluminescence dynamics by time-correlated single-photon counting (TCSPC), samples (solutions in glass vials) were excited

by a train of 532 nm, 100 ps-duration pulses at a repetition rate of 100 kHz generated by a laser diode (PicoQuant; LDH-P-FA-530B). The considerable waiting time between pulses (10 μs) ensured that the delayed fluorescence – consistent with long-lived 'trap' states on the nanocrystals – decayed below the noise floor of the detector ($<10^{-3}$ of the peak signal under these conditions). The pump was attenuated to yield roughly 1 nW of average excitation power, with a roughly 20 μm diameter excitation spot at the sample. Under these low-fluence excitation conditions, the photoluminescence decay dynamics were independent of excitation intensity. Accordingly, we consider bimolecular recombination channels to be unimportant.

The emission from the nanocrystals was collected and imaged onto an InGaAs/InP single-photon counting avalanche photodiode (Micro Photon Devices; $IR-DH-025-C), fitted with a long-pass filter (Chroma Technology Corp.; EP900LP) to suppress the scattered photons from the visible pump. The detector was operated asynchronously from the laser source, with a 2 MHz gate frequency and a 90% duty cycle. Using a PicoQuant PicoHarp and standard software, a decay trace histogram was generated by correlating the times of detection events with the proximal trigger from the pump laser. The time resolution, judged from the onset of the response to unfiltered pump scatter, was ~300 ps. This stemmed primarily from the uncertainty in the detector response at the low over-voltages required for low-noise operation. After verifying that no rapid dynamics were observed, 256 ps time bins were used during data collection.

Animal procedures

Animal model and cell line—Murine Gl261 cells (Gl261 WT) were originally provided by the Frederick National Laboratory (NCI, Frederick, MD). Gl261-GFP-Gluc cell line was generated by transducing Gl261 WT cells with a bicistronic lentivirus vector (under the control of the constitutive cytomegalovirus promoter) containing both green-fluorescent-protein (GFP) and Gaussian-luciferase (GFP-Gluc) genes separated by an internal ribosomal entry site element[43], provided by the MGH vector core. All cells were grown in serum free conditions using the NeuroCult NS-A proliferation kit (Stemcell technologies, Vancouver, Canada) and maintained in a humidified atmosphere of 5% CO_2 and 95% air at 37°C. Gl261-GFP-Gluc cells were repeatedly tested negative for mycoplasma using the Mycoalert Plus Mycoplasma Detection Kit (Lonza) and authenticated before use by IDEXX laboratories (North Grafton, MA).

Approximately 200,000 tumor cells were implanted stereotactically into the left striatum of 8—10 week old male C57BL/6 mice (Gl261-GFP-Gluc) 2 mm left of the sagittal suture, 0.1 mm rostral of the bregma and at 2 mm depth from the brain surface[44,45]. Intravital images were taken through cranial windows.

Cold exposure to activate brown adipose tissue—Mice were housed at 22°C with ad libitum access to standard laboratory chow diet. Cold exposure (4°C) was performed in single cages for 24 h. We used male 12 weeks old C57BL/6 (Charles River Laboratory) wild-type mice, which were fasted for the last 4 h before the imaging experiment. For *in vivo* imaging to measure metabolic rates mice were anesthetized and SWIR QD-labeled

lipoproteins were injected via a tail vein catheter with a syringe pump (at a rate of 13.3 μL/min).

Animal experiments were conducted in accordance with approved institutional protocols of MGH and MIT.

SWIR imaging apparatus

Macroscopic imaging setup—For macroscopic imaging from above or below, we used two configurations of a single custom-built setup.

We coupled a 10 W 808 nm laser (Opto Engine; MLL-N-808) in a 910 μm-core metal-cladded multimode fiber (Thorlabs; MHP910L02). The output from the fiber is passed through a ground-glass plate (Thorlabs; DG20-220-MD) to provide uniform illumination over the working area. The excitation flux in this configuration is around 15mW/cm^2. The working area is comprised of a plate of clear glass affixed atop four 1 in pillars, 6 in off the table for illumination from above or 12 in off the table for illumination from below.

We used a 4 in square first-surface silver mirror (Edmund Optics; Part No 84448) to direct the emitted light through various filters (Thorlabs, Edmund Optics) to a Princeton Instruments Nirvana equipped with various C-mount camera lenses (Navitar). The whole assembly was surrounded by a partial enclosure to eliminate excess light while enabling manipulation of the field of view during operation.

For imaging of the vasculature of the brain through skin and skull we used a custom build setup to lenses (Thorlabs AC254-100-C and AC254-75-C) with a 1" silver elliptical mirror (Thorlabs PFE10-P01) and different long- and bandpass filters (Thorlabs and Edmund Optics) in between.

Microscopic imaging setup—We used a Nikon Ti-E inverted microscope equipped with a Stage UP Kit (Nikon) and a backport adaptor. For illumination we used a 808 nm laser diode coupled to a fiber which was attached to the backport adaptor. To eliminate laser speckle we used an optune speckle remover (Edmund Optics; 88-397). We used a dichroic filter (Thorlabs; DMLP900R) to direct the excitation light to the sample and a 1000 nm longpass filter (Thorlabs; FELH1000,) to select the emission light. Imaging was done with a 10× (Nikon; CFI Plan Apo Lambda) or a 2× (Nikon; CFI Plan Apo Lambda,) objective. The PI Nirvana camera was attached to the sideport of the microscope. The camera was cooled to −80°C for imaging, the AD conversion rate was set to 10 MHz, the gain set to high, with different exposure times resulting in different frame rates.

Metabolic imaging with functionalized SWIR QDs

The mice were prepared as described in this report. For the resulting images we defined regions of interest representing the tail injection site, interscapular brown adipose tissue (BAT), and liver. The total intensity contained within each region of interest was determined and used to produce the time series data. A constant background was removed from each time series, based on the intensities of background fluorescence at the beginning of injection.

To fit the signal from the BAT, we identified the time point when the injection was halted, and noted the intensity of the signal from that point to the end of the experiment. We modeled the signal as a sum of three exponential functions, two of which had positive amplitude representing loss of signal, and a third with negative amplitude representing residual gain of signal due to the injection.

Fluorescence angiography

We used our microscopic imaging setup with the 2× objective to image the brain of a mouse with a cranial window. We recorded a video (30fps) of the brain during injection of PEGylated QDs, three days after a similar injection to pre-label the tumor. Using this video we can perform a form of principal component analysis (PCA), using the PoissonNMF ImageJ plugin[46]. This method identifies the extent to which each pixel can be represented as an artery or vein by relating its temporal profile to those of vessels of known identity. Any signal existing before the imaged injection was assigned to be the background and pre-labeled tumor, from which we removed a laser speckle artifact by a form of flat field correction by combining multiple pictures taken with different fields of view before the injection. The color image in Figure 5e represents the overlay of pre-injection, artery, and vein characters.

Multiphoton microscopy

Fluorescein isothiocyanate–dextran/phosphate buffered saline solution (FITCDextran) was prepared for in vivo vessel tracing in a concentration of 10 mg/mL. Following tail vain injection of 100 μL of FITC-Dextran, a vessel image was acquired using multiphoton imaging described previously[44] on a custom-built multiphoton laser-scanning microscope using confocal laser-scanning microscope body (Optical Analysis Corp.; Olympus 300) and a broadband femtosecond laser source (Spectra-Physics; High Performance MaiTai). Image slices were taken with 300 mW at a wavelength of 810 nm. Imaging studies were performed with a 20× magnification, 0.95NA water immersion objective (Olympus XLUMPlanFl, 1-UB965, Optical Analysis). Image analysis was carried out using ImageJ.

Particle image velocimetry

The PIV code was written in Matlab 2015a and is available here: https://github.com/massivehair/PIV

Firstly, the image stack is segmented into two regions, one containing flow and the other, background. This is achieved by first smoothing every frame in the stack using a Gaussian smoothing kernel with a sigma parameter of 2 pixels. The standard deviation of each X,Y position in the stack is taken, as a measure of the amount of motion in that part of the image. Finally, a grayscale image erosion operation using a disk kernel with a diameter of 25 pixels is used to reduce the influence of noisy pixels and isolated high-variance regions of the image. A threshold could then be selected to distinguish flowing regions from background. Since the effect of this threshold (and the prior steps) is to reduce the computational load of calculating large areas in which there is no flow, the algorithm is not especially sensitive to the choice of smoothing kernel, or threshold that is too low; any errors will simply reduce

computational efficiency. For the data presented in Figure 7 c and d thresholds of 0.05 and 0.1 were used respectively.

To perform the PIV calculation, firstly, each frame is smoothed using a Wiener filter with a filter size of 5 pixels on a side. A window size and maximum step size are defined. In the case of the data presented in Figure 7 the window size is 8 pixel and the step size 40 pixel. Flow is calculated at grid locations spaced by the window size, provided these locations contain flow information (as assessed by the threshold previously applied). To calculate flow, two sub-images are taken from consecutive frames. One is taken from the first frame, centered on each grid location, with a size given by the window size. The second is taken from the subsequent frame, centered on the same grid location, with a size equal to the sum of the window size and the maximum step size. A cross-correlation is then taken between the two sub-frames; this is termed the correlation map. This is repeated for every grid locations, resulting in n-1 correlation maps for each, where n is the number of frames in the stack.

Correlation maps were averaged across all frames, following the method of Meinhart, Wereley and Santiago[47], and then the peak corresponding to the modal flow vector located using a three-point Gaussian estimator[48].

Supplementary Material

Refer to Web version on PubMed Central for supplementary material.

Acknowledgments

This work received support from the NIH in part through 5-U54-CA151884 (M.G.B.), P01-CA080124 (R.K.J. and D.Fukumura), R35 CA197743, P50 CA165962 and R01-CA126642 (R.K.J.), R01-CA096915 (D.Fukumura), the NIH funded Laser Biomedical Research Center through 4-P41-EB015871-30 (M.G.B.), and NCI/Federal Share Proton Beam Program Income (R.K.J.); National Foundation for Cancer Research (RKJ), and Warshaw Institute for Pancreatic Cancer Research and MGH Executive Committee on Research (D.Fukumura); the ARO through the Institute for Soldier Nanotechnologies (W911NF-13-D-0001; J.A.C., O.C., H.W., G.W.H., M.G.B.); the Department of Defense through DoD W81XWH-10-1-0016 (R.K.J.); and the NSF through ECCS-1449291 (D.Franke, M.G.B.). This work was supported as part of the MIT Center for Excitonics, an Energy Frontier Research Center funded by the U.S. Department of Energy, Office of Science, Office of Basic Energy Sciences under Award Number DE-SC0001088 (T.S.B., M.W.B.W.). O.T.B. is supported by an EMBO long-term fellowship. A.B. is supported by a Deutsche Forschungsgemeinschaft Research Fellowship (BA 4925/1-1). D.Franke is supported by a fellowship of the Evonik Stiftung and fellowship of the Boehringer Ingelheim Fonds. This research was conducted with government support under and awarded by the Department of Defense, Air Force Office of Scientific Research, National Defense Science and Engineering Graduate Fellowship 32 CFR 168a (J.A.C.). J.H. is supported by a grant from the Fondation Leducq - Triglyceride Metabolism in Obesity and Cardiovascular Disease. L.R. received a Mildred Scheel Fellowship (Deutsche Krebshilfe). D.K.H. and D.M.M. were supported by NSF GRFP fellowships. J.K. was supported by fellowships from the Deutsche Forschungsgemeinschaft and the SolidarImmun Foundation. CJR and PTCS acknowledge support from NIH 4-P41-EB015871-30, DP3-DK101024 01, 1-U01-NS090438-01, 1-R01-EY017656-0, 6A1, 1-R01-HL121386-01A1, the Biosym IRG of Singapore-MIT Alliance Research and Technology Center, the Koch Institute for Integrative Cancer Research Bridge Initiative, Hamamatsu Inc., and the Samsung GRO program.

We thank Sylvie Roberge and Peigen Huang for technical assistance. We also thank QDVision for providing an InAs/CdZnS QD sample (InAs-016) used in this study. We are grateful to Gökhan Hotamisligil for critical discussion and continuing support.

References

1. de Jong M, Essers J, van Weerden WM. Imaging preclinical tumour models: improving translational power. Nat. Rev. Cancer. 2014; 14:481–493. [PubMed: 24943811]
2. Welsher K, et al. A route to brightly fluorescent carbon nanotubes for near-infrared imaging in mice. Nat. Nanotechnol. 2009; 4:773–80. [PubMed: 19893526]
3. Yi H, et al. M13 phage-functionalized single-walled carbon nanotubes as nanoprobes for second near-infrared window fluorescence imaging of targeted tumors. Nano Lett. 2012; 12:1176–83. [PubMed: 22268625]
4. Hong G, et al. Through-skull fluorescence imaging of the brain in a new near-infrared window. Nat. Photonics. 2014; 8:723–730. [PubMed: 27642366]
5. Ghosh D, et al. Deep, noninvasive imaging and surgical guidance of submillimeter tumors using targeted M13-stabilized single-walled carbon nanotubes. Proc. Natl. Acad. Sci. U. S. A. 2014; 111:13948–53. [PubMed: 25214538]
6. Bardhan NM, Ghosh D, Belcher AM. Carbon nanotubes as in vivo bacterial probes. Nat. Commun. 2014; 5:4918. [PubMed: 25230005]
7. Welsher K, Sherlock SP, Dai H. Deep-tissue anatomical imaging of mice using carbon nanotube fluorophores in the second near-infrared window. Proc. Natl. Acad. Sci. U. S. A. 2011; 108:8943–8. [PubMed: 21576494]
8. Hong G, et al. Multifunctional in vivo vascular imaging using near-infrared II fluorescence. Nat. Med. 2012; 18:1841–6. [PubMed: 23160236]
9. Naczynski DJ, et al. Rare-earth-doped biological composites as in vivo shortwave infrared reporters. Nat. Commun. 2013; 4:2199. [PubMed: 23873342]
10. Lim YT, et al. Selection of quantum dot wavelengths for biomedical assays and imaging. Mol. Imaging. 2003; 2:50–64. [PubMed: 12926237]
11. Hong G, et al. Ultrafast fluorescence imaging in vivo with conjugated polymer fluorophores in the second near-infrared window. Nat. Commun. 2014; 5:4206. [PubMed: 24947309]
12. Tsukasaki Y, et al. Short-Wavelength Infrared Emitting Mutimodal Probe for Non-Invasive Visualization of Phagocyte Cell Migration in Living Mice. Chem. Commun. 2014; 50:14356–9.
13. Tao Z, et al. Biological imaging using nanoparticles of small organic molecules with fluorescence emission at wavelengths longer than 1000 nm. Angew. Chem. Int. Ed. Engl. 2013; 52:13002–6. [PubMed: 24174264]
14. Dong B, et al. Facile Synthesis of Highly Photoluminescent Ag 2 Se Quantum Dots as a New Fluorescent Probe in the Second Near-Infrared Window for in Vivo Imaging. Chem. Mater. 2013; 25:2503–2509.
15. Zhu C-N, et al. Ag_2Se quantum dots with tunable emission in the second near-infrared window. ACS Appl. Mater. Interfaces. 2013; 5:1186–9. [PubMed: 23380909]
16. Zhang YY, et al. Ag2S quantum dot: a bright and biocompatible fluorescent nanoprobe in the second near-infrared window. ACS Nano. 2012; 6:3695–702. [PubMed: 22515909]
17. Tsukasaki Y, et al. Synthesis and optical properties of emission-tunable PbS/CdS core–shell quantum dots for in vivo fluorescence imaging in the second near-infrared window. RSC Adv. 2014; 4:41164–41171.
18. Chen O, et al. Compact high-quality CdSe-CdS core-shell nanocrystals with narrow emission linewidths and suppressed blinking. Nat. Mater. 2013; 12:445–51. [PubMed: 23377294]
19. Franke D, et al. Continuous injection synthesis of indium arsenide quantum dots emissive in the short-wavelength infrared. Nat. Commun. 2016; :12749.doi: 10.1038/ncomms12749 [PubMed: 27834371]
20. Zhang Y, et al. Biodistribution, pharmacokinetics and toxicology of Ag2S near-infrared quantum dots in mice. Biomaterials. 2013; 34:3639–46. [PubMed: 23415643]
21. Dubertret B, et al. In vivo imaging of quantum dots encapsulated in phospholipid micelles. Science. 2002; 298:1759–62. [PubMed: 12459582]
22. Stroh M, et al. Quantum dots spectrally distinguish multiple species within the tumor milieu in vivo. Nat. Med. 2005; 11:678–82. [PubMed: 15880117]

23. Bruns OT, et al. Real-time magnetic resonance imaging and quantification of lipoprotein metabolism in vivo using nanocrystals. Nat. Nanotechnol. 2009; 4:193–201. [PubMed: 19265850]
24. Bartelt A, et al. Brown adipose tissue activity controls triglyceride clearance. Nat. Med. 2011; 17:200–5. [PubMed: 21258337]
25. Heeren J, Bruns O. Nanocrystals, a new tool to study lipoprotein metabolism and atherosclerosis. Curr. Pharm. Biotechnol. 2012; 13:365–72. [PubMed: 21470118]
26. Fay F, et al. Nanocrystal Core Lipoprotein Biomimetics for Imaging of Lipoproteins and Associated Diseases. Curr. Cardiovasc. Imaging Rep. 2013; 6:45–54. [PubMed: 23687557]
27. Jung C, et al. Intraperitoneal Injection Improves the Uptake of Nanoparticle-Labeled High-Density Lipoprotein to Atherosclerotic Plaques Compared With Intravenous Injection: A Multimodal Imaging Study in ApoE Knockout Mice. Circ. Cardiovasc. Imaging. 2014; 7:303–11. [PubMed: 24357264]
28. Jacobs GH, Neitz J, Deegan JF. Retinal receptors in rodents maximally sensitive to ultraviolet light. Nature. 1991; 353:655–6. [PubMed: 1922382]
29. Henry, L., Foster, J., David Small, James, G., Fox, E. The Mouse in Biomedical Research: Normative Biology, Immunology, and Husbandry. Elsevier Science; 2014.
30. Berndt, A., Leme, AS., Paigen, B., Shapiro, SD., S, K. Mouse Phenome Database web site. The Jackson Laboratory; Bar Harbor, Maine USA: Unrestrained plethysmograph and anesthetized forced oscillation methods of measuring lung function in 29 inbred strains of mice. MPD:35108. http://phenome.jax.org
31. Hillman EMC, Moore A. All-optical anatomical co-registration for molecular imaging of small animals using dynamic contrast. Nat. Photonics. 2007; 1:526–530. [PubMed: 18974848]
32. Kamoun WS, et al. Simultaneous measurement of RBC velocity, flux, hematocrit and shear rate in vascular networks. Nat. Methods. 2010; 7:655–660. [PubMed: 20581828]
33. Adrian RJ. Twenty years of particle image velocimetry. Exp. Fluids. 2005; 39:159–169.
34. Adrian RJ. Particle-Imaging Techniques for Experimental Fluid Mechanics. Annu. Rev. Fluid Mech. 1991; 23:261–304.
35. Shi Y, Cheng JC, Fox RO, Olsen MG. Measurements of turbulence in a microscale multi-inlet vortex nanoprecipitation reactor. J. Micromechanics Microengineering. 2013; 23:75005.
36. Schindelin J, et al. Fiji: an open-source platform for biological-image analysis. Nat. Methods. 2012; 9:676–82. [PubMed: 22743772]
37. Aharoni A, Mokari T, Popov I, Banin U. Synthesis of InAs/CdSe/ZnSe core/shell1/shell2 structures with bright and stable near-infrared fluorescence. J. Am. Chem. Soc. 2006; 128:257–64. [PubMed: 16390155]
38. Li JJ, et al. Large-scale synthesis of nearly monodisperse CdSe/CdS core/shell nanocrystals using air-stable reagents via successive ion layer adsorption and reaction. J. Am. Chem. Soc. 2003; 125:12567–75. [PubMed: 14531702]
39. Hines MA, Scholes GD. Colloidal PbS Nanocrystals with Size-Tunable Near-Infrared Emission: Observation of Post-Synthesis Self-Narrowing of the Particle Size Distribution. Adv. Mater. 2003; 15:1844–1849.
40. Pietryga JM, et al. Utilizing the lability of lead selenide to produce heterostructured nanocrystals with bright, stable infrared emission. J. Am. Chem. Soc. 2008; 130:4879–85. [PubMed: 18341344]
41. Supran GJ, et al. High-Performance Shortwave-Infrared Light-Emitting Devices Using Core–Shell (PbS–CdS) Colloidal Quantum Dots. Adv. Mater. 2015; 27:1437–42. [PubMed: 25639896]
42. Folch J, Lees M, Sloane Stanley GH. A simple method for the isolation and purification of total lipides from animal tissues. J. Biol. Chem. 1957; 226:497–509. [PubMed: 13428781]
43. Wurdinger T, et al. A secreted luciferase for ex vivo monitoring of in vivo processes. Nat. Methods. 2008; 5:171–3. [PubMed: 18204457]
44. Kodack DP, et al. Combined targeting of HER2 and VEGFR2 for effective treatment of HER2-amplified breast cancer brain metastases. Proc. Natl. Acad. Sci. U. S. A. 2012; 109:E3119–27. [PubMed: 23071298]

45. Kloepper J, et al. Ang-2/VEGF bispecific antibody reprograms macrophages and resident microglia to anti-tumor phenotype and prolongs glioblastoma survival. Proc. Natl. Acad. Sci. U. S. A. 2016; 113:4476–81. [PubMed: 27044098]

46. Neher RA, et al. Blind source separation techniques for the decomposition of multiply labeled fluorescence images. Biophys. J. 2009; 96:3791–800. [PubMed: 19413985]

47. Meinhart CD, Wereley ST, Santiago JG. A PIV Algorithm for Estimating Time-Averaged Velocity Fields. J. Fluids Eng. 2000; 122:285.

48. Marxen M, Sullivan PE, Loewen MR, Èhne BJ, Jähne B. Comparison of Gaussian particle center estimators and the achievable measurement density for particle tracking velocimetry. Exp. Fluids. 2000; 29:145–153.

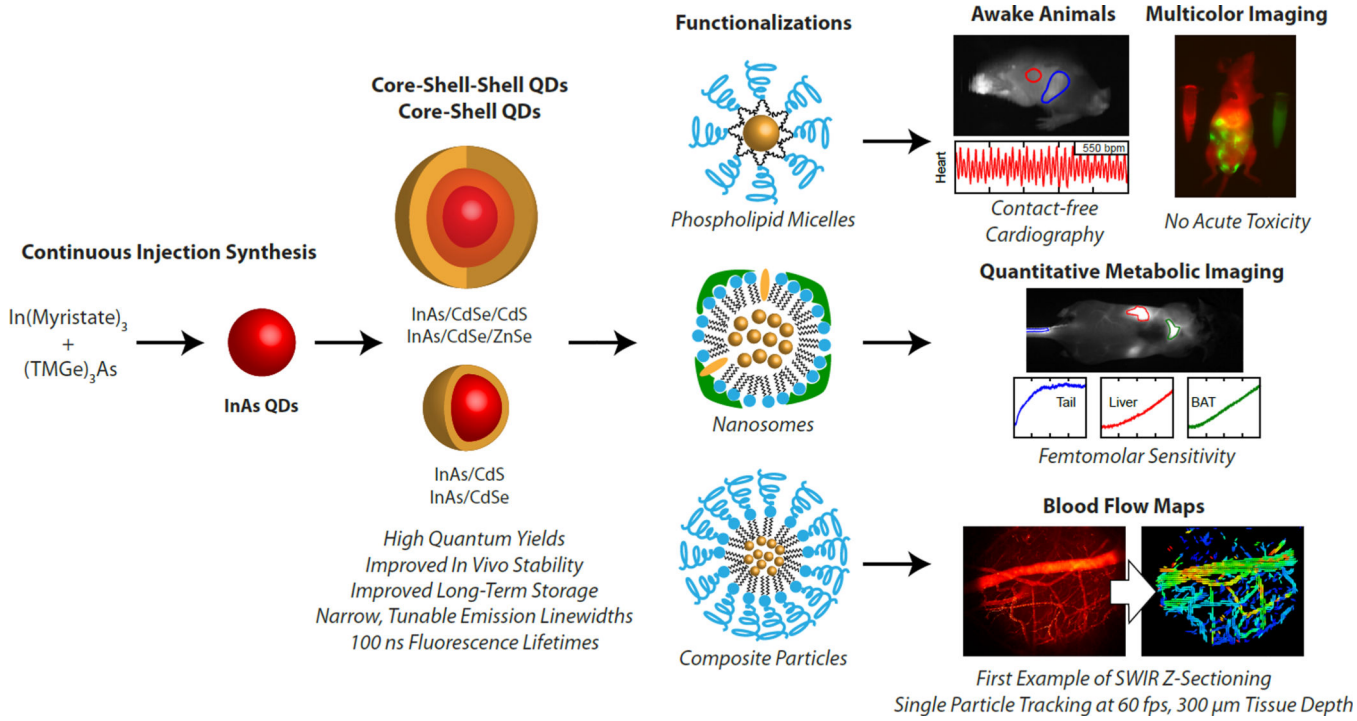

Figure 1. Short-wave infrared quantum dots for next generation *in vivo* optical imaging

A schematic overview of the synthesis of core/shell and core/shell/shell SWIR quantum dots and the subsequent functionalization for next generation imaging applications is shown. InAs QDs are synthesized via continuous injection approach which allows for improved nanocrystal growth over long time at high reaction temperatures. Subsequently InAs core QDs are overcoated with various shell materials to allow for a further red-shift and fine-tuning of the emission. The class of synthesized core-shell (CS) and core-shell-shell (CSS) QDs are then functionalized via three distinct surface coatings that tailor the physiological properties for specific SWIR imaging applications.

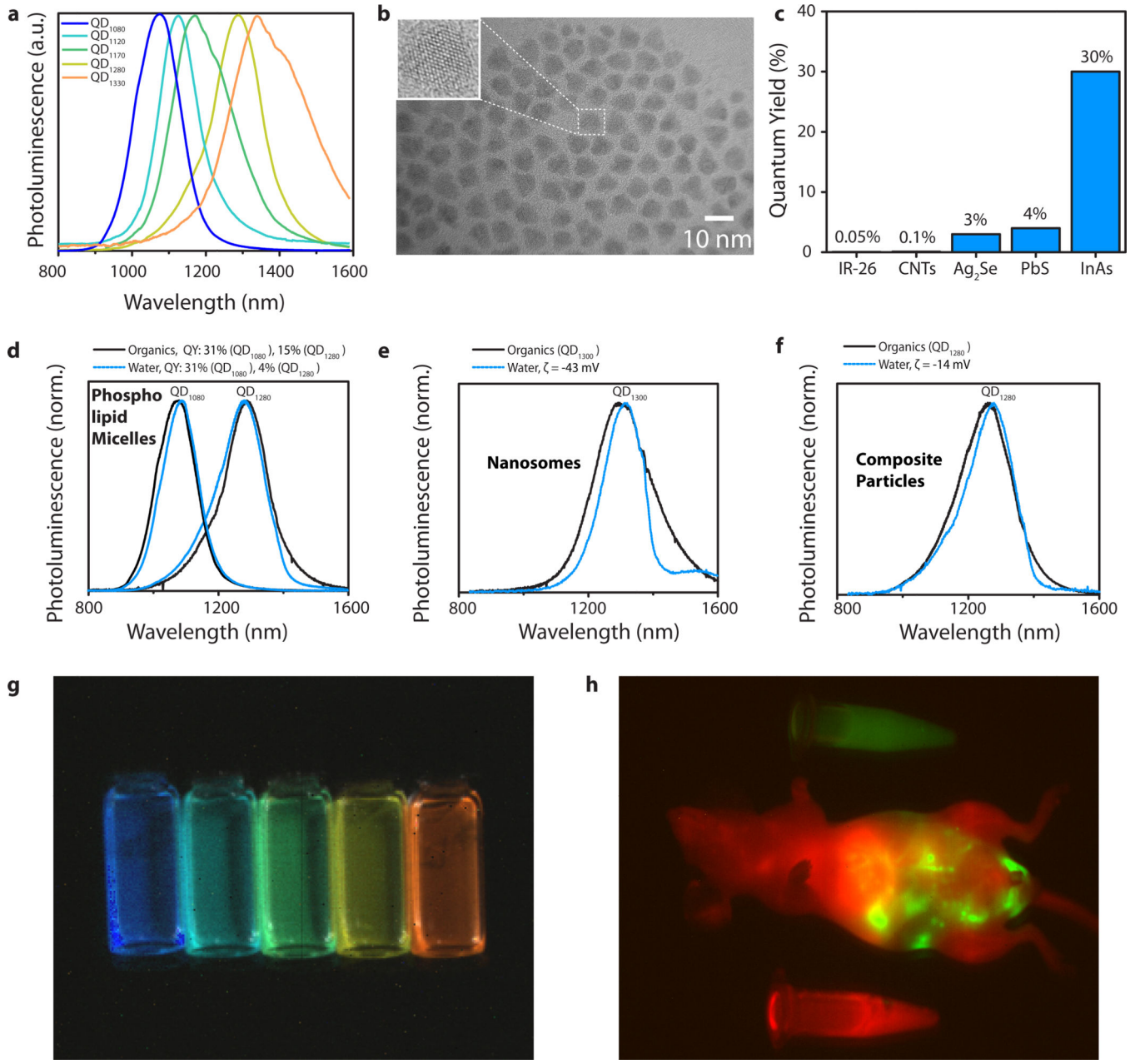

Figure 2. InAs core/shell quantum dots with high quantum yield and size-tunable emission for functional and high-speed SWIR imaging

Spectra of five different core/shell and core/shell/shell SWIR QDs are shown (QD_{1080}: $InAs(CdSe)_1(ZnSe)_3$, QD_{1120}: $InAs(CdSe)_{1.5}$, QD_{1170} $InAs(CdSe)_3$, QD_{1280}: $InAs(Cd_{0.9}Zn_{0.1}S)$, QD_{1330} $InAs(CdSe)_6$) (a). A representative TEM of core/shell/shell SWIR QDs shows monodisperse nanoparticles with a diameter of 7 nm and a narrow size distribution of 8% (b). Core/shell and core/shell/shell SWIR QDs exhibit a quantum yield in aqueous buffer of up to 30%, much higher than for previously-used materials (c). The emission spectra remain unaffected after transfer into aqueous buffer from organic solvent for PEGylated SWIR QDs ($\zeta = -12$ mV for QD_{1300}) (d), nanosomes with SWIR QDs (e) and PEGylated SWIR QD composite particles (f). Note that water has a very strong

absorption band around 1450 nm which can be recognized as a feature caused by reabsorption through the solvent in the three spectra. A spectral image of the five samples shown in (a) yields a pseudo-color SWIR image (g). Two different SWIR QDs were injected into a nude mouse intraperitoneally (green) and intravenously (red). A spectral image was taken and separated into red and green by linear unmixing (h).

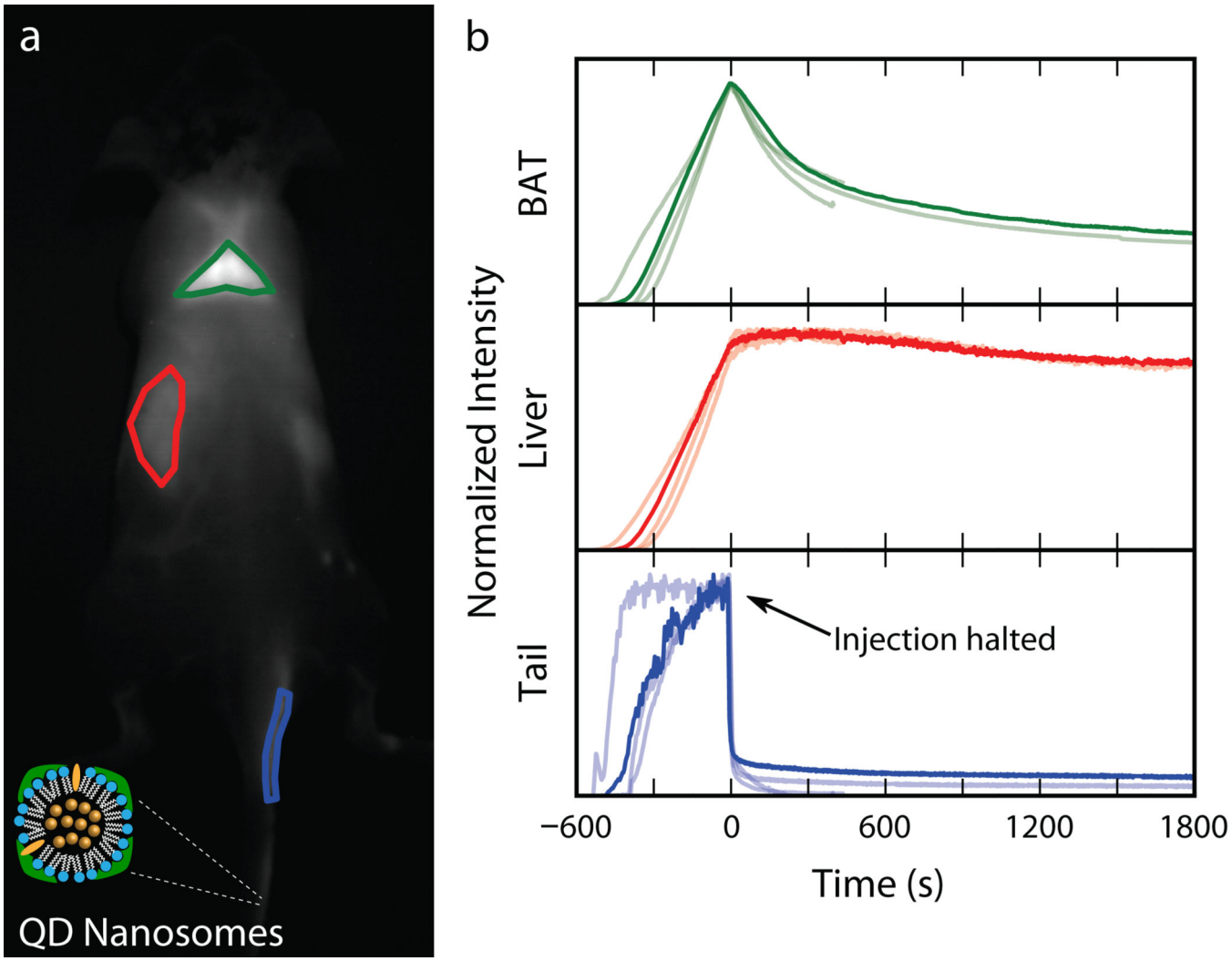

Figure 3. QD nanosomes for metabolic imaging

(a) A solution of a SWIR QD labeled recombinant chylomicrons was injected at a constant rate (26.7 μL/min or 0.267 mg triglycerides/min) into the tail vein of a cold-exposed mouse. The mouse was illuminated using an 808 nm laser with 15 mW/cm^2, and the SWIR emission was measured for the brown adipose tissue (BAT), liver and tail vein. (b) This process was repeated for four mice, with the darkened curves representing the results from the one mouse shown in (a), and the lighter curves showing the qualitative similarity of the other mice. The BAT signal after the injection revealed two distinct timescales for clearance: the initial signal loss is consistent with binding and release (about 3 minute time constant, 50% of the signal), while the longer-term component is consistent with uptake (>30 minute time constant).

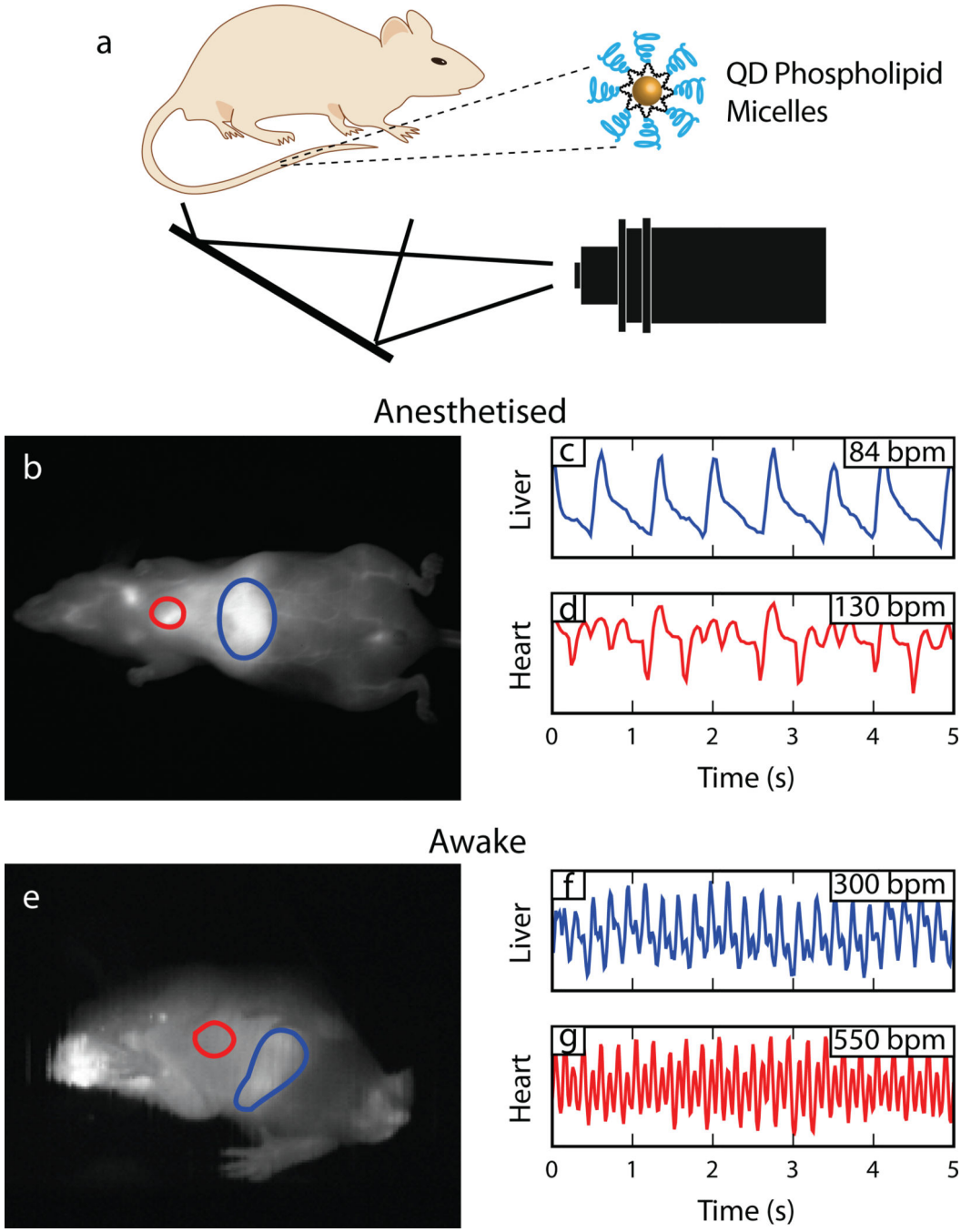

Figure 4. High-speed SWIR imaging for contact free monitoring of heart and respiratory rate in anesthetized and awake mice using QD phospholipid micelles

Imaging in ventral orientation (a) at video-rate (30 fps; Supplementary Video 4) with SWIR QDs (808 nm excitation) allows imaging vital signs like heart rate (red ROI) and respiration (blue ROI). (b) The respiratory rate of this anesthetized mouse is 84 breaths per minute (c) and the heart rate is 130 beats per minute (d). The bright emission of our SWIR QDs allows the imaging of an awake mouse (66.5 fps; Supplementary Video 5) and the detection of the signal fluctuations generated by motion of liver and heart (e). A respiratory rate of 300

breaths per minute (f) and a heart rate of 550 beats per minute (g) is observed in this awake but resting mouse.

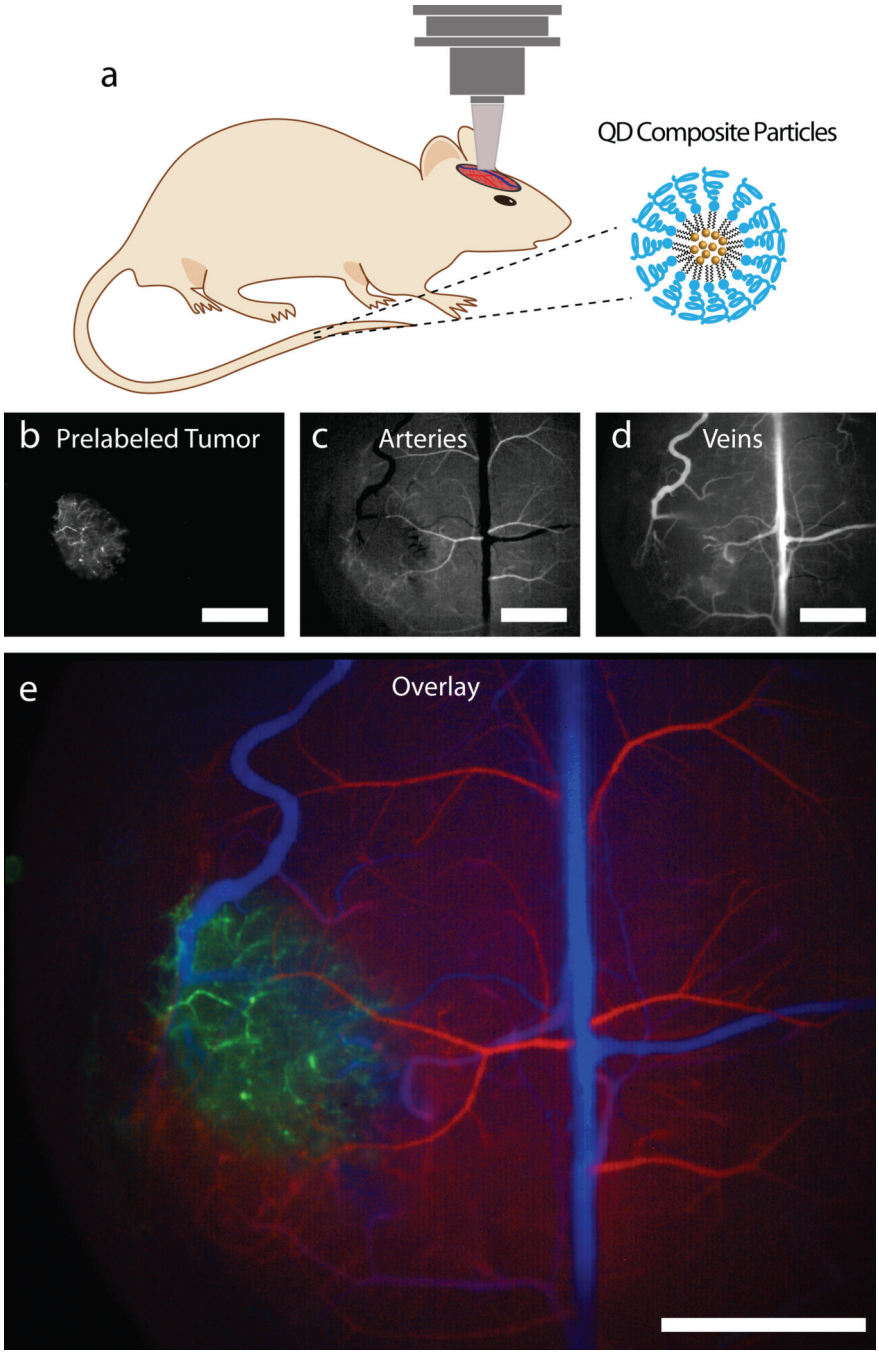

Figure 5. High-speed intravital imaging using QD composite particles

SWIR intravital imaging (808 nm excitation, 1000nm long pass for emission) in a mouse with a cranial window (a) bearing a glioblastoma multiforme (GBM) in the left hemisphere of the brain as shown in (b). Principal component analysis (PCA) was used to distinguish arterial (c) from venous vessels (d) in the brain. This information is color-coded creating a multicolor angiograph (e) showing the abnormalities of the tumor microvascular network as opposed to normal arterial/venous brain vasculature (green: tumor; red: arterial vessels; blue: venous vessels). Scale bars are 1500 μm.

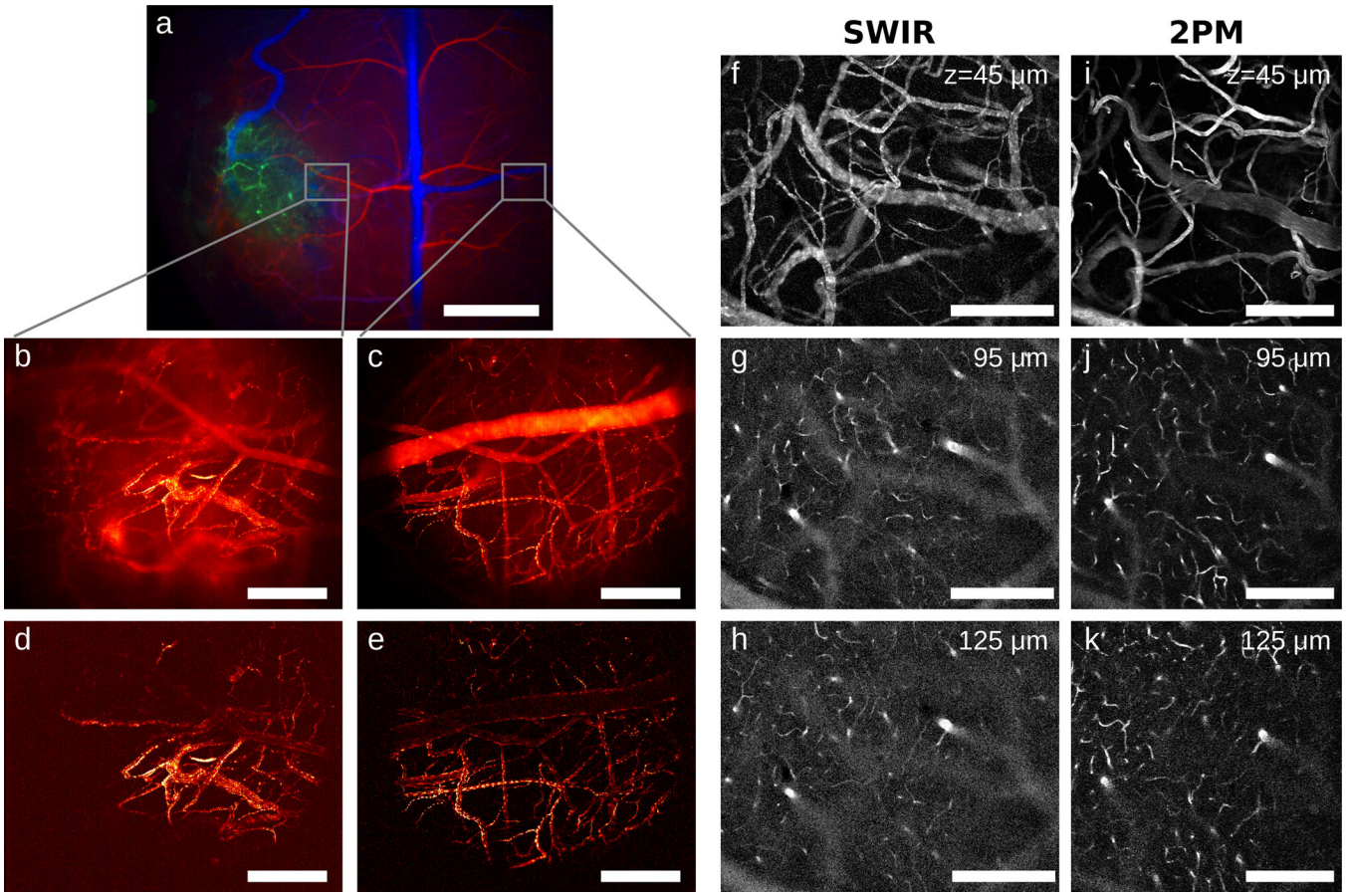

Figure 6. High resolution high-speed intravital imaging using QD composite particles

In addition to generating a multicolor angiography image of a glioblastoma tumor in a cranial window model (a) high-resolution high-speed QD-SWIR imaging at 60 fps was used to image the vascular network of the tumor margin (b) and to compare it to the vasculature in the contralateral hemisphere (c). Maximum intensity projections of 600 frames over 10 seconds are shown here. By subtracting the average signal of these 600 frames from the maximum intensity projection the signal originating only from individual QD-SWIR composite particles in the focus was isolated. This allowed isolating blood flow from the focal plane of the tumor margin (d) and the vessels on the contralateral lateral side (e). To enhance the contrast of the focal plane and provide true z-sectioning capability, we calculated the sum of the magnitude of the difference of each frame from the average, which is sensitive only to fluctuations over time, i.e. the transit of individual composite particles. **Figures 6f–k** directly compare the micrographs of the same fields of view of a healthy mouse brain at various depths taken by our z-sectioning approach (f—i) and conventional multiphoton microscopy (i—k). Scale bars in b—e are 300 µm, and in f—k are 200 µm. Scale bar for (a) is 1500 µm, scale bars for (b—e) are 300 µm and scale bars for (f—k) are 200 µm.

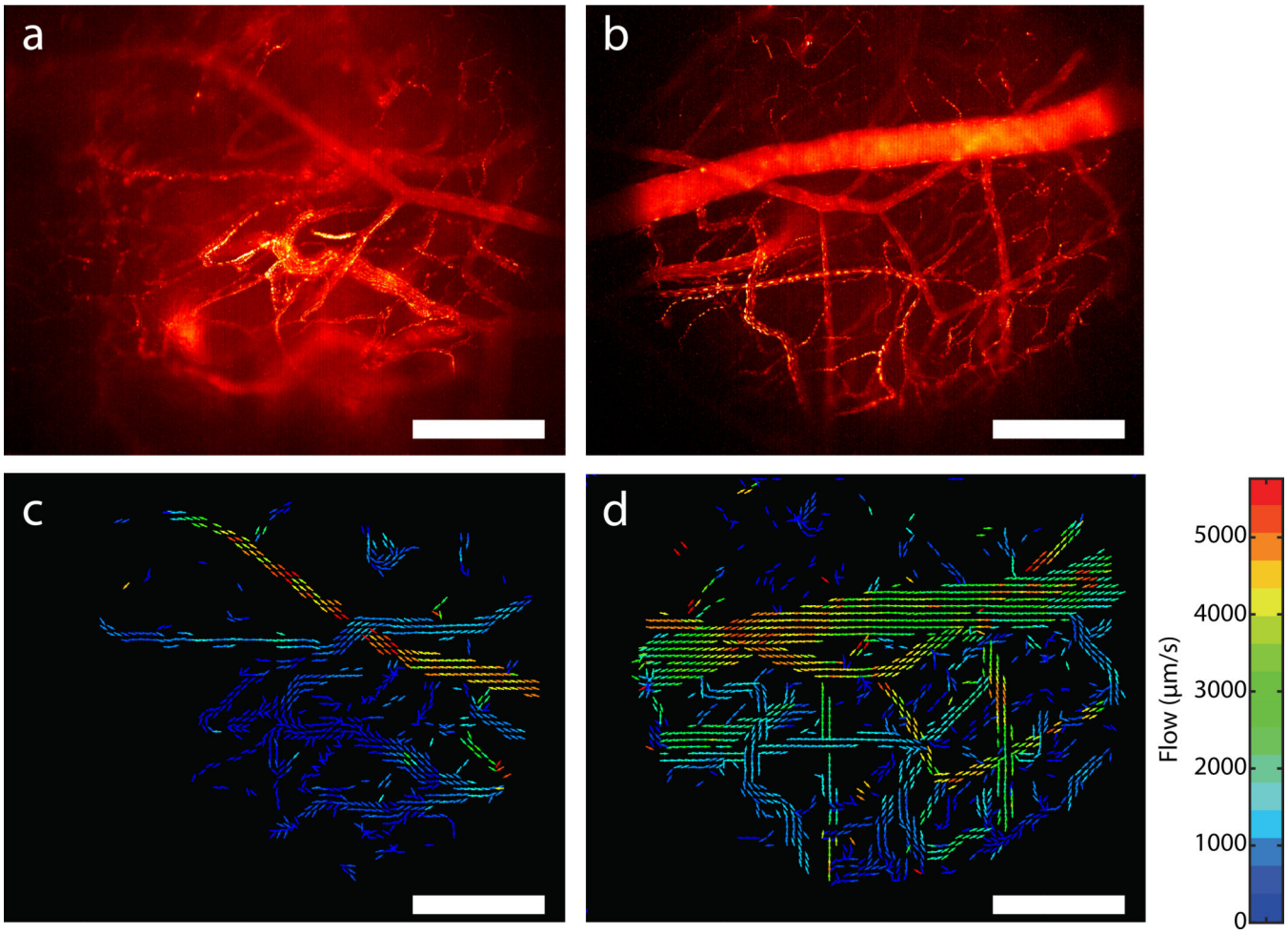

Figure 7. High resolution high-speed SWIR intravital imaging to generate flow maps of microvascular networks using QD composite particles

Applying a multi-pass particle image velocimetry (PIV) approach in the tumor margin and the healthy hemisphere (as shown in Figure 6b,c) generates a flow map for each slice (c and d). All scale bars are 300 μm, and the units for velocity are μm/s.